IEEE Access
Multidisciplinary | Rapid Review | Open Access Journal

Received August 22, 2019, accepted September 12, 2019, date of publication September 17, 2019, date of current version October 2, 2019.

Digital Object Identifier 10.1109/ACCESS.2019.2941990

A Novel Approach for Breast Cancer Investigation and Recognition Using M-Level Set-Based Optimization Functions

GAMAL G. N. GEWEID[1,2], (Member, IEEE), AND MAHMOUD A. ABDALLAH[3], (Member, IEEE)
[1]Electrical Engineering Department, School of Electrical Engineering and Computer Science, University of North Dakota, Grand Forks, ND 58202, USA
[2]Electrical Engineering Department, Benha Faculty of Engineering, Benha University, Benha 13511, Egypt
[3]Manufacturing Engineering Department, Central State University, Wilberforce, OH 45384, USA

Corresponding author: Gamal G. N. Geweid (gamal.geweid@und.edu)

ABSTRACT Breast cancer identification is the first and foremost step in the journey of proper diagnosis and treatment of this disease. Therefore, many medical examinations and applications are devised and used including different approaches for breast imaging. For medical image analysis, nonparametric algorithm has been used. This work focuses on improving breast cancer recognition in mammogram images using a nonparametric approach based on image pixel intensities (IBCNP). A nonparametric approach is a new expression to deal with uncertainty. In this paper, the nonparametric approach is used to solve the uncertainty in breast cancer detection; uncertainty means no one knows for sure how to detect breast cancer without imaging, which creates an uncertainty for the oncologists. This paper investigates the feasibility of applying the nonparametric approach in mammography (x-ray breast imaging) to detect and hence diagnose and treat breast cancer. Analysing breast images is a very complicated process and requires distinguishing normal and malignant pixel intensities. Maximizing the shared data between image pixel intensities and the desired areas (infected region) is defined as the identification problem, subject to a constraint on the total size of the desired area borders. As part of this research, a comparative study was conducted on the proposed algorithm, Breast Cancer Cells Infestation based on a set of partial differential equations (PDEs), Incoherent Motion in Breast Cancer (IMBC), Global Dynamics of a Breast Cancer Competition Model using five simple differential equations (SDFs), and Estimation of Intensity Using Nonparametric Method (EINP) techniques. These five techniques of medical image segmentation are applied to 156 different mammogram images to obtain the exact measurement of the efficiency of the identification process. This process uses multiple performance metrics such as the overall mammogram image quality (Q), the dice similarity coefficient (DSC), Peak signal-to-noise ratio (PSNR) metric, Haussdorff Distance (HD), and probability of tumor detection (PTD). This paper assumes lack of knowledge of the probability densities in relation to pixel intensities of an image within a given area. It proposes an estimation of non-parametric density that formulates the theoretical data optimization problem by applying curve evolution methods and deriving the correlated gradient flows. It uses level-set techniques to achieve the resulting evolution. The algorithm was applied to 156 sets of different mammogram images from twelve groups with both malignant and/or normal. The experimental findings showed that the proposed algorithm is 94.937% accurately effective in breast cancer detection.

INDEX TERMS Mammograms image, pixel intensities, nonparametric technique, breast cancer detection.

I. INTRODUCTION

Breast cancer is considered as one of the main health concerns amongst women around the world. Prevalence of breast cancer has increased lately. This issue is particularly critical given inadequate public health awareness. Recent statistics [1] show that breast cancer is one of the top causes of malignant-related deaths amongst women at the age of 40-70 years. Therefore, it is crucial to best utilize imaging systems and laboratory analysis in order to accurately identify breast cancer. When a breast cancer is detected early, there is a higher chance for proper treatment. Hence, it is highly

The associate editor coordinating the review of this manuscript and approving it for publication was Sudipta Roy.

This work is licensed under a Creative Commons Attribution 4.0 License. For more information, see http://creativecommons.org/licenses/by/4.0/

important that new effective methods are introduced and developed to detect and investigate breast cancer in early stages. Accurate identification of breast cancer tissues in early stages leads to increase survival rate and save many people live.

In the first stage of diagnosis, a very critical procedure in image analysis is sampling that is present in multiple implementations, like format identification, object discovery, and categorization in medical imaging. Image sampling has many methods in order to enhance the quality, and it has multiple uses categorized by an assortment of functions concerned by the intensity of pixels. In such method, distinct objects have distinct oscillation disseminations that they are distinguished according to the regular and average divergence of each dissemination.

Several research groups attempted to develop a mathematical model for breast cancer (Abernathy *et al.* [2], Cho *et al.* [3], Knútsdóttir *et al.* [4], and Simmons *et al.* [5]). Simmons, Alex, Pamela Burrage, Sunil, and Kevin presented a brief survey of breast cancer, and mathematical modelling and simulation roles in separating apart the underlying biophysical procedures [5]. Knútsdóttir et al. introduced a set of partial differential equations (PDEs) to determine the aggregation conditions [4]. In that work, the authors used cell-based discrete 3D simulation to track the movement and fates of individual cells through aggregation. The linear stability analysis of the PDE model shows that a reduction in chemotaxis density, and chemical secretion of cells or an increase in chemical degradation in the model could prevent the cells spontaneous aggregation. Discrete model simulations show that the ratio of tumor cells to macrophages in aggregates rises when the epidermal growth factor (EGF) secretion parameter is improved. Cho et al. compared the sampling strategies and fitting methods, including the implementation of enhanced b-value selection for optimized estimation of intra voxel incoherent indication parameters in breast cancer [3].

Abernathy introduced a system of five simple differential equations (SDFs) that take into account population dynamics of tumor cells, cancer stem-cells, and healthy ones [2]. To ensure the determination of the cancer in the absence of the immune cells, the author obtained adequate conditions on the values of the parameters, and when the immune response is included, elimination of the cancer occurs.

Colom et al. presented a non-parametric technique that estimates noise depending on the intensity and frequency of an image [6]. The noise model was evaluated on image pixels and can be used consistently in all pixel-based noise reduction techniques. The technique was applied to cases where the image noise pattern in scanned photos and JPEG images were not allowed. The image noise model and its evaluation method were validated by comparing the approximations with the true-ground curve associated with the raw and JPEG images. De-noising experiments on digitized images have confirmed the effectiveness of the evaluation technique. Diamantas et al. introduced a technique based on a single static camera to solve the problem of background subtraction [7]. In addition to the practical sharpness of foreground motion objects, background scenes were an important stage in tracking and classifying objects in dynamic and complex environments.

The technique is based on the sequential average of the distinct pixels on a small learning sample and the pixel density modeling with a log-Normal intensity function that gives the greatest convulsions of the divergence among the background pixels. Schwartz proposed a technique for capturing changes in aerial images taken at different times in a scene, possibly with dissimilar cameras and from different points of view. This is a crucial stage for computer vision and other image processing applications such as visual surveillance, remote sensing and civil infrastructure [8]. Unlike most pixel-based approaches, that study combines contextual data and core density evaluations to model and recognize changes in the image areas.

Image segmentation is done based on different techniques (Ronneberger *et al.* [9], Farag *et al.* [10], and Salem *et al.* [11]). Segmentation methods which can be classified based on functions applied to the intensity value of the pixel in the desired image exist. The main concept of these techniques is that different frequency distributions of different objects can be distinguished according to mean and standard deviation (Chini *et al.* [12], Zhou *et al.* [13], and Niu *et al.* [14]).

A network and training strategy are based on the intensive use of data development to make data more efficient is presented in (Ronneberger *et al.* [9] and Jordan *et al.* [15]). The architecture has a narrowing path to capture context, and a symmetrical extension path allows accurate position. A computerized bottom-up technique was introduced for pancreas identification in calculated tomography images, Farag *et al.* [10] and Taruttis and Ntziachristos [16]). The technique generates cascade of hierarchical data dissemination by categorizing image areas on dissimilar resolutions and (segments) super pixels. It introduces a partition-based hierarchical approach, which transforms the parameters of the distribution of two classes to different sizes of tiles [12]. In order to resolve the problem of geographic stability, a global reference control scheme was introduced to filter incorrect matches for copy recognition because it ignores the global reference information of local institutions [13].

A new regional model of division of objects or structures in images was demonstrated in a window based on a local intensity differences spatial distances to improve segmentation results [14]. The technique uses local similarity factor to extract the object margin while ensuring certain noise robustness [17]. Spatial pattern recognition and characterization of Ni concentrations was presented using digital image processing for signs of Ni Topasol concentrations in Europe [15], where moving average smoothing was applied to the TIN-interpolated grid model to remove small irregularities. Emerging technology and recent biological and emerging advances and potential clinical applications were displayed in [16].

There are many other techniques for image segmentation, such as artificial neural networks, Mumford-Shah (global optimization techniques), Region of Interested Growing (edge-based detection), and nonparametric approaches based on curve evaluation technique.

Gardezi, S. J. S., Elazab, A., Lei, B., & Wang, T. x (18) presented an overview of Machine learning (ML) and Deep Learning (DL) approaches with particular application for breast cancer, which has a significant impact on the diagnostic abilities of the Computer-Aided Design (CAD) systems. They have used the Science databases, MEDLINE, Springer, and Google Scholar in literature survey regarding Breast Cancer Detection and Diagnosis Using Mammographic data. In addition, they have captured studies in deep learning for the past 5 years that have used mammogram dataset (18). In the study, they found that heterogeneous breast densities make masses more challenging to identify and classify compared with calcifications (18).

Li, H., Mendel, K. R., Lan, L., et al., (19) discussed the classification of breast cancer in digital mammography. In the study, they focused on improving breast lesion classification with digital mammography by using automatic lesion segmentation and radiomic analysis. They applied radiomic texture analysis to normal areas of interest in mammogram to evaluate the mammographic parenchymal patterns (19).The area under the receiver operating characteristic curve is used to calculate the classification performance of Bayesian artificial neural network classifier for differentiating between malignant and benign lesion (19).

Junior, G. B., da Rocha, S. V., et al., (20) discussed breast cancer detection in mammography using geostatistics, spatial diversity, and concave geometry. In their work, six radiological features were selected (spiculation, margin sharpness, size, roundness of all tumor characteristics and asymmetry and beta power of the parenchymal feature set) over 50% of the time during of the selection process of the characteristics in the set of combined characteristics (20). They evaluated the detection rate of each entity extraction using the Bearer vector device in the Mini-Mammographic Database (MIAS), Digital Database for Screening Mammography (DDSM) databases, with 74 and 621 mammograms respectively, which contain at least one mass region. The classification performance is calculated by using the detection rate of malignant tissue and false-positive rate for MIAS and DDSM database (20).

In this paper, an improved non-parametric method is used to discover breast cancers in medical images, with the presence of very limited information about the demographical attributes of the interesting discovery districts. The proposed approach includes the mutual information and nonparametric density assessment, regarding the computation of bar-chart, variations, averages to determine the covariation arrays. The medical image under consideration is split into multiple unclassified zones with distinct densities, which are not known a priori, the issue related to nonparametric density assessments is interpreted. Using curve assessment to set quantity of curves amongst the unclassified zones afterwards, with every curve splitting the region of the image into two zones: internal zone and external zone. Then, the mutual information is calculated. The energy function is computed as multiphase zone is calculated, and the inclination drift calculation of the image boundary is viewed to check the location. Finally, the sampled medical image is obtained.

The proposed nonparametric approach is an accurate and reliable technique. The resulting topographies were processed using the method proposed by the paper, and then compared with other methods. Such comparison showed that the suggested algorithm is more accurate and faster. When applied to many sets, the algorithm spotted the exact location and size of breast cancer.

This paper is organized as follows: Section II presents basic information of the proposed approach. Section III shows curve evaluation approach that is based on energy function optimization, Section IV illustrates the multiphase mammogram segmentation technique, the regions of interest segmentation using level-set functions and the performance evaluation of mammogram segmentation methods. The experimental results are presented in section V, using medical images with real data and distribution varieties. Section VI presents the case study of the proposed technique to the medical images while the discussions of results shown in section VII. Section VIII illustrates the performance evaluation and comparative results. Finally, Section IX concludes the paper.

II. SEGMENTATION OF BREAST REGION IN MAMMOGRAM

A. MAMMOGRAM BOUNDARY IDENTIFICATION

The proposed technique segments the image under test into sets of regions based on pixel intensity levels in foreground and background. The mammogram image is divided into n-regions according to intensity levels for each region, where $G_1, G_2, \ldots, G_n$ signify the real unidentified areas, and the intensity value at pixel y, signified by $G(y)$, is pulled from the u_i if $u_i \in G_i$, where u_is are unidentified densities. The target of segmenting the mammogram image by curve estimation is to move a set of curves $\left\{\vec{C}_1, \ldots, \vec{C}_m\right\}$ (consistently, a level- set functions $\{Q_1, \ldots, Q_m\}$) so that these curvatures divide the mammogram domain into the real areas $G_1, G_2, \ldots, G_n$. Each curvature C_i divides the mammogram domain into two regions: the region inside the curve and outside the curve. Consequently, the M-set of level functions will segment mammogram image into 2^m zones, each of which is represented by marking of the M-set of level functions in that section. For instance, if m = 2, the four regions $G_{++}, G_{+-}, G_{-+}, G_{--}$ are as shown in Fig. 1.

The image pixel intensities is submitted as redundant zones procedure $F(y)$ with pixel index as a collection of multiple topologically different elements based on intensity levels for each region, as shown in Fig.2. The N-area image sampling and the curve development approach are used to draw a curve $\vec{C}$ touching the boundary between G_i and G_j, the

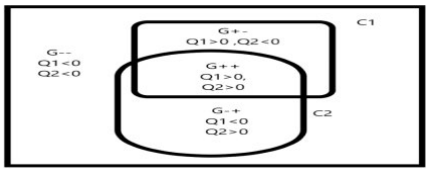

FIGURE 1. The areas $G_{++}, G_{+-}, G_{-+}, G_{--}$ divided by the curves$(\vec{C}_1, \vec{C}_2)$.

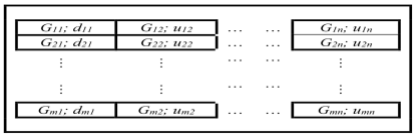

FIGURE 2. Explanation of n-regions, and the associated distributions (G_{mn}, u_{mn}).

internal area of the curve G_+ intersects at G_i and the external area intersects at G_j. $\vec{C}$ s function of t, time ingredient that can be ignored, $\vec{C} = \vec{C}(t)$. This splitting of the image region produces a binary-label $L_{\vec{C}}(y) : G \to \{L_+, L_-\}$, which is an ingredient of the mammogram region G to a set of two labels $\{L_+, L_-\}$. $L_{\vec{C}}(x) = L_+$ if $y \in G_i$ and $L_{\vec{C}}(y) = L_-$ if $y \in G_j$.

B. MAMMOGRAM INTENSITY RECOGNITION

This section introduces the mutual data (MD) between the label and the image intensity and discusses its properties. Given the areas divided by the curves $C \triangleq \left\{\vec{C}_i\right\}_{i=1}^{m}$, every pixel in the mammogram is signified by y label, $L - C.(y)$. Also, a label $L_C : G \to \left\{L_{s(i+)}, L_{s(i-)}\right\}$.

$$L_C(y) = L_{s(i+)} \text{ if } y \in G_{s(i+)}, \quad 1 \le i \le 2^{m-1} \tag{1}$$

$$L_C(y) = L_{s(i-)} \text{ if } y \in G_{s(i-)}, \quad 2^{m-1} + 1 \le i \le 2^m \tag{2}$$

where $s(i+)$ is the i_{th} element in the set-level $\{L_{++\cdots+}, \cdots, L_{+-\cdots-}\}$ and $s(i-)$ is the i_{th} element in the set-level $L_{++\cdots+} \cdots, L_{+-\cdots-}\}$. The proposed technique uses nonparametric approach to categorize image pixels into sets of areas with different intensity level. This method can identify the defected areas in mammogram by calculating the value of m depends on the number of high-intensity regions in the mammogram image. For example, if m=3, then there are eigh areas $G_{+--}, G_{++-}, G_{+-+}, G_{+--}, G_{-++}, G_{-+-}, G_{--+}\ G_{---}$ as shown in Fig. 3.

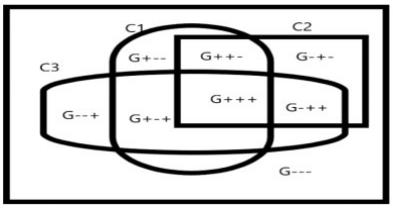

FIGURE 3. Explanation of the curves and intersection between them.

A pixel Yin G is randomly selected such that Y is a regularly circulated random position in the mammogram domain and the label $L_{\vec{C}}(y)$ is a random parameter that is based on the curvature $\vec{C}$ [21]–[24]. The values $L_{s(i+)}$ and $L_{s(i-)}$ are taken with probability $\left|G_{s(i+)}\right| / |G|$ and $\left|G_{s(i-)}\right| / |G|$, respectively, where $\left|G_{s(i+)}\right|$ signifies the area of the section $G_{s(i+)}$. Furthermore, the mammogram intensity $G(Y)$ is a random parameter that is based on the real sections G_i, and has the following density [21], [25]:

$$u_{G(y)}(w) = \sum_{i=1}^{n} P_r(Y \in G_i) u_{F(Y)|Y \in G_i}(w) = \sum_{i=1}^{n} \frac{|G_i|}{|G|} u_i(w) \tag{3}$$

where w is a pretext for the densities. $P_{F(Y)}$ is a combination of $u_i s$ due to the randomness of the pixel position Y. The improbability of a pixel position being in G_i, signifies the improbability of the intensity assumed at the pixel position. The label $L_{\vec{C}}(Y)$ includes some data about the previous improbability, specifically Y, being in G_i or G_j. Subsequently, the label $L_{\vec{C}}(Y)$ can precisely decide whether $Y \in G_i$ if less improbability $G(Y)$ is developed, or additional details concerning $F(Y)$ the description will have. The reciprocal data $M\left(F(Y) : L_{\vec{C}}(Y)\right)$ is used as a criterion of segmentation [26]. The mutual data is formally considered as

$$\begin{aligned} M\left(F(Y) : L_{\vec{C}}(Y)\right) &= k(F(Y)) - k\left(F(Y) \,|\, L_{\vec{C}}(Y)\right) \\ &= k(F(Y)) - \sum_{i=1}^{2^m} P_r\left(L_{\vec{C}}(Y) = L_{s(i+)}\right) \\ &\quad \times k\left(F(Y) \,|\, L_{\vec{C}}(Y) = L_{s(i+)}\right) \\ &\quad \times \sum_{i=2^{m-1}+1}^{2^m} P_r\left(L_{\vec{C}}(Y) = L_{s(i-)}\right) \\ &\quad \times k\left(F(Y) \,|\, L_{\vec{C}}(Y) = L_{s(i-)}\right) \end{aligned} \tag{4}$$

where $k(W)$ is the difference in entropy of a random variable W with support S and is calculated by:

$k(W) = -\int_S u_W(w) \log u_W(w) dw$ [27], [28]. Three entropies in equation (2) are functions of $u_{F(Y)}$, $u_F(Y)|L_{\vec{C}}(Y) = L_{s(i+)}$ and $u_{F(Y)|L_{\vec{C}}(Y)=L_{s(i+)}}$, respectively. The two restricted distributions are determined as follows

$$\begin{aligned} &u_{F(Y)|L_{\vec{C}}(Y)=L_{s(i+)}}(w) \\ &= \sum_{i=1}^{n} P_r\left(Y \in G_i \,|\, L_{\vec{C}}(Y) = L_{s(i+)}\right) u_{F(Y)|A \in G_i, L_{\vec{C}}(Y)=L_{s(i+)}}(w) \\ &= \sum_{i=1}^{n} \frac{\left|G_{s(i+)} \cap G_i\right|}{\left|G_{s(i+)}\right|} u_i(w) \end{aligned} \tag{5}$$

$$\begin{aligned} &u_{F(Y)|L_{\vec{C}}(Y)=L_{s(i-)}}(w) \\ &\sum_{i=1}^{n} P_r\left(Y \in G_i \,|\, L_{\vec{C}}(Y) = L_{s(i-)}\right) u_{F(Y)|Y \in G_i, L_{\vec{C}}(Y)=L_{s(i-)}}(w) \\ &= \sum_{i=1}^{n} \frac{\left|G_{s(i-)} \cap G_i\right|}{\left|G_{s(i-)}\right|} u_i(w) \end{aligned} \tag{6}$$

Each dependent entropy calculates the heterogeneity degree in each zone given by the curve $\vec{C}$. The more similar the segmented regions, the greater the shared data, and the restricted entropies, which is a qualified property for segmentation [27], [28]. The mutual data is exploited if and only if it is the true segmentation, if, $G_{s(i+)} = G_i$, $G_{s(i-)} = G_j$ (or,

equivalently $G_{s(i-)}= G_i$, $G_{s(i+)}= G_j$). Practically, we cannot calculate the mutual data $M\left(F\left(Y\right) : L_{\vec{C}}\left(Y\right)\right)$ because the above computations included in the sections G_i and G_j, and pixel intensities u_i and u_j are unknown to us [16], [18], [25].

In energy functionality, mutual data should be weighted by the image area to represent the over-all mutual data between the label and the image, since $M\left(F\left(Y\right); L_{\vec{C}}\left(P\right)\right)$ matches to the influence of one pixel to the over-all information. The subsequent energy is computed by

$$E\left(\vec{C}\right) = -\left|G\right| \hat{M}\left(F\left(Y\right); L_{\vec{C}}\left(Y\right)\right) + a \oint_{\vec{C}} ds \tag{7}$$

where $\oint_{\vec{C}} ds$ is the total curve length and a is a scalar factor.

III. CURVE EVALUATION APPROACH BASED ON ENERGY FUNCTION OPTIMIZATION

This section presents the derivation of the formula for the curve evaluation to lessen the energy function. First, the evaluation of the restricted entropy conditions is illustrated using the Parzen intensity evaluations based on non-parametric [25], [29]. Then, the gradient flow for $E\left(\vec{C}\right)$ is determined.

A. DIFFERENTIAL ENTROPY EVALUATION

Equation (4) is used to estimate the differential entropies. Since $\hat{k}(G\left(Y\right))$ in equation (4) is independent of the curvature size, we see:

$$\begin{aligned}
&\hat{k}\left(F\left(Y\right) | L_{\vec{C}}\left(Y\right) = L_{s(i+)}\right) \\
&\quad = -\frac{1}{\left|G_{s(i+)}\right|} \int_{G_{s(i+)}} log\, \hat{u}_{s(i+)}\left(F\left(Y\right)\right) dy \\
&\quad = -\frac{1}{\left|G_{s(i+)}\right|} \int_{G_{s(i+)}} \log\left(\frac{1}{\left|G_{s(i+)}\right|} \int_{G_{s(i+)}} \mathrm{V}\left(\mathrm{F}\left(\mathrm{y}\right)\right.\right. \\
&\qquad \left.\left. - \mathrm{F}(\hat{\mathrm{y}})\right) \mathrm{d}\hat{\mathrm{y}}\right) \mathrm{dy}
\end{aligned} \tag{8}$$

It was found that $k\left(F\left(Y\right) | L_{\vec{C}}\left(Y\right) = L_{s(i+)}\right)$ contains the predictable value of the approach of $u_{s(i+)} \triangleq u_{F(Y)|L_{\vec{C}}(Y)=L_{s(i+)}}$, and using the kernel $(w) = \left(1/\sqrt{2\pi b^2}\right) e^{-w^2/2b^2}$, where b is a scalar factor

$$\begin{aligned}
&\hat{k}\left(F\left(Y\right) | L_{\vec{C}}\left(Y\right) = L_{s(i-)}\right) \\
&\quad = -\frac{1}{\left|G_{s(i-)}\right|} \int_{G_{s(i-)}} \log \hat{u}_{s(i+)}\left(F\left(Y\right)\right) \\
&\quad = -\frac{1}{\left|G_{s(i-)}\right|} \int_{G_{s(i-)_-}} \log\left(\frac{1}{\left|G_{s(i-)}\right|} \int_{G_{s(i-)}} V\left(F\left(y\right)\right.\right. \\
&\qquad \left.\left. - F(\hat{y})\right) d\hat{y}\right) dy
\end{aligned} \tag{9}$$

Consequently, equations (8) and (9) have nested region integrals. This work assumes an object inside a larger one so that the desired region is an integral of the form

$$E\left(\vec{C}\left(t\right)\right) = \int_G f\left(\varepsilon\left(y, t\right)\right) du \tag{10}$$

where $\varepsilon\left(y, t\right) = \int_G g(y, \hat{y}) d\hat{y}$ and g does not based on $\vec{C}$ [21], [30], G is the range within the curvature $\vec{C}$. Therefore, the integral of the area declines more quickly and is given by

$$\frac{\partial \vec{C}}{\partial t} = -\left[f\left(\varepsilon\left(\vec{C}\right)\right) + \int_G f'\left(\varepsilon\left(y\right)\right) g(y, \vec{C}) dy\right] \vec{n} \tag{11}$$

where $\vec{n}$ is the unit vector outwardly. Note that $f\left(\varepsilon\left(y, t\right)\right)$ in equation (10) depends on the curve length $\vec{C}$.

B. MUTUAL DATA EVALUATION USING NONPARAMETRIC TECHNIQUE

The nonparametric estimation of the reciprocal information in the form of overlapping zone, as in equations (8) and (9), is possible to easily assess using the overall energy function (gradient-flow) $E\left(\vec{C}\right)$ of equation (7). The $E\left(\vec{C}\right)$ is written as:

$$E\left(\vec{C}\right) = -\left|G\right| \hat{k}\left(F\left(Y\right)\right) + E_-\left(\vec{C}\right) + E_+\left(\vec{C}\right) + a \oint_{\vec{C}} ds \tag{12}$$

where the components $E_-\left(\vec{C}\right)$ and $E_+\left(\vec{C}\right)$ are given by

$$\begin{aligned}
E_-\left(\vec{C}\right) &= \sum\nolimits_{i=2^{m-1}+1}^{2^m} E_{s(i-)}\left(\vec{C}\right); \\
E_+\left(\vec{C}\right) &= \sum\nolimits_{i=1}^{2^{m-1}} E_{s(i+)}\left(\vec{C}\right). \\
E_{s(i+)}\left(\vec{C}\right) &= \left|G\right| P_r\left(L_{\vec{C}}\left(Y\right) = L_{s(i+)}\right) \\
&\quad \times k\left(F\left(Y\right) | L_{\vec{C}}\left(Y\right) = L_{s(i+)}\right) \\
&= -\int_{G_{s(i+)}} \log\left(\frac{1}{\left|G_{s(i+)}\right|} \int_{G_{s(i+)}} V\left(F\left(y\right)\right.\right. \\
&\quad \left.\left. - F(\hat{y})\right) d\hat{y}\right) dy
\end{aligned}$$

Subsequently, $1/\left|G_{s(i+)}\right|$ is based on the curvature, E_+ are separated into two integrals. The gradient flow for E_+ is computed as:

$$E_{s(i+)} = E^1_{s(i+)} + E^2_{s(i+)} \tag{13}$$

where

$$E^1_{s(i+)} = -\int_{G_{s(i+)}} \log\left|G_{s(i+)}\right| dy = -\left|G_{s(i+)}\right| \mathrm{Log}\left|G_{s(i+)}\right|,$$

and

$$E^2_{s(i+)} = \int_{G_{s(i+)}} \log\left(\int_{G_{s(i+)}} V\left(F\left(y\right) - F\left(\vec{C}\right)\right) d\hat{y}\right) dy.$$

The gradient flow for $E^2_{s(i+)}$ is $\nabla_{\vec{C}} E^2_{s(i+)}$, given by:

$$\begin{aligned}
\nabla_{\vec{C}} E^1_{s(i+)} &= -\nabla_{\vec{C}}\left|G_{s(i+)}\right| \log\left|G_{s(i+)}\right| - \nabla_{\vec{C}}\left|G_{s(i+)}\right| \\
&= \left(1 + \log\left|G_{s(i+)}\right|\right) \vec{n}
\end{aligned} \tag{14}$$

$$\nabla_{\vec{C}} E^1_+ = \sum\nolimits_{i=1}^{2^{m-1}} \left(1 + \log\left|G_{s(i+)}\right|\right) \vec{n}.$$

$$\nabla_{\vec{C}} E_+ = \nabla_{\vec{C}} E^1_+ + \nabla_{\vec{C}} E^2_+ \tag{15}$$

where

$$\nabla_{\vec{C}} E_+ = \sum_{i=1}^{2^{m-1}} \left[-1 + \log u_{s(i+)} \left(F(\vec{C}) \right) + \frac{1}{|G_{s(i+)}|} \int_{G_{s(i+)}} \frac{V(F(y) - F(\vec{C}))}{\hat{u}_{s(i+)}(F(y))} dy \right] \vec{n},$$

$$\nabla_{\vec{C}} E_- = \sum_{i=2^{m-1}+1}^{2^m} \left[1 - \log u_{s(i-)} \left(F(\vec{C}) \right) - \frac{1}{|G_{s(i-)}|} \int_{G_{s(i-)}} \frac{V(F(y) - F(\vec{C}))}{\hat{u}_{s(i-)}(F(y))} dy \right] \vec{n}.$$

Then the gradient flow for $E\left(\vec{C}\right)$ of (12) is obtainable as follows:

$$\frac{\partial \vec{C}}{\partial t} = \sum_{i=1}^{2^{m-1}} \left[\log u_{s(i+)} \left(F(\vec{C}) \right) + \frac{1}{|G_{s(i+)}|} \int_{G_{s(i+)}} \frac{V(F(y) - F(\vec{C}))}{\hat{u}_{s(i+)}(F(y))} dy \right] \vec{n} - \sum_{i=2^{m-1}+1}^{2^m} \left[\log u_{s(i-)} \left(F(\vec{C}) \right) + \frac{1}{|G_{s(i-)}|} \int_{G_{s(i-)}} \frac{V(F(y) - F(\vec{C}))}{\hat{u}_{s(i-)}(F(y))} dy \right] \vec{n} - ak\vec{n} \quad (16)$$

where $-ak\vec{n}$ is the gradient-flow for the length of the curvature and k is the curve dimensions [21], [30].

In each iteration, the number of calculation takes pixels $O(A(|G_+| + |G_-|) + |G_+|^2 + |G_-|^2 + A(|G_+| + |G_-|) \sim O\left((number\ of\ pixels)^2\right)$ [21], where A is the total pixels on the curvature (the narrow-band size) [21], [30]. The calculation of the first term at the set of pixels along the curvature takes $O(A(|G_+| + |G_-|))$ time, the second term takes $O\left(|G_+|^2\right)$ time to calculate and store $\hat{u}_+(F(y))$ for all $y \in G_+$ and the computation of the integration at the set of points on the curvature takes $O(M|R_+|)$ time. Also, the third term takes $O(|G_+|^2 + M|R_+|)$ [25], [31].

To reduce the computational complexity time, fast Gauss transform (FGT) can be used to calculate density estimates based on B pixels information in the form of $u(y) = (1/B)\sum_{i=1}^{B} V(y - y_i)$ at A different pixels in $O(c(A + B))$ time instead of $O(AB)$ time and c is the number of accuracies which are created with the desired accuracy of the proposed approach [21], [28]. If B pixels from G_+ is chosen to calculate $\hat{u}_+$ and select another B pixels from G_-, the computational process in every iteration is $O(c(A + B + B) + c(B + B) + c(A + B) + c(B + B) + c(A + B))$ by using the FGT in case of two region, if there are m curves so 2^m of regions are found. The complexity will be more complicated. In equation (16) the calculation of integration of the second and the third part takes $O(c(A + B))$ time. B is selected as a linear function of A due to the narrow band size. The differentiable of the equation (16) is div $\left((g(y, y)\nabla Q_l / |\nabla Q_l|)\right)|\nabla Q_l|$ changed from the bend of the curvature flow, where Q_l is the proper set of level function [9].

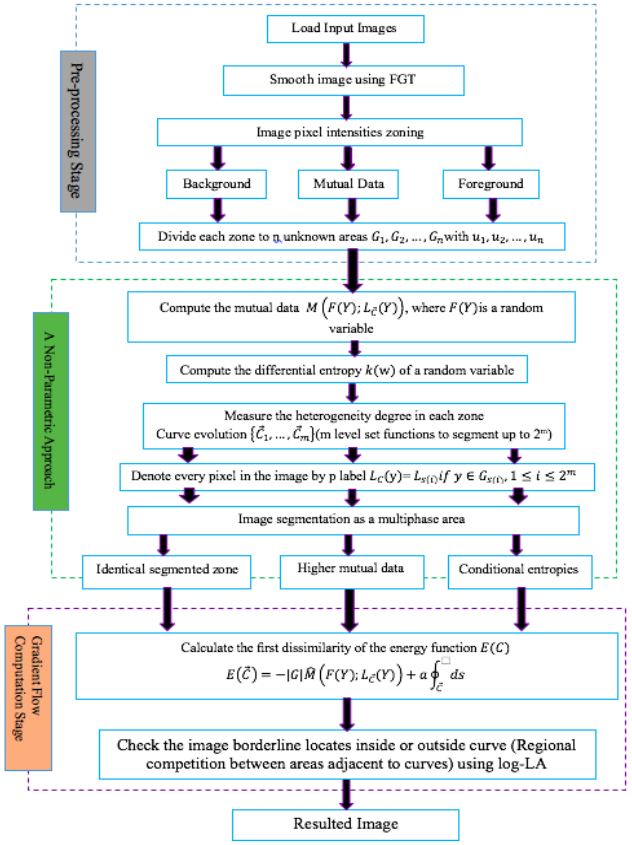

FIGURE 4. The algorithm of non-parametric approach based on image pixel intensities.

A log-LA is the first part of the differentiable equation (16) which is equivalent to the supposition that the intensity of the detected mammogram $F(\vec{C})$ at a specified pixel on the active border goes to the back-ground region, $G--$. or the foreground region, $G-+$ based upon the existing estimations of the distributions, $u-+$. and u_-. The integrations of the pixels on the contour using log-LA term to identify which of the regions are in the desired image are identical.

IV. MULTIPHASE MAMMOGRAM SEGMENTATION TECHNIQUE

This section introduces the proposed segmentation technique to the mammogram images with more than two objects (infected areas). In this approach, m level-set functions are used to segment the mammogram into 2^m regions, and the equation of the resulting estimation curve is established to be a real generalization of nonparametric region rivalry as shown in Fig. 4.

A. REGIONS OF INTEREST SEGMENTATION USING LEVEL-SET FUNCTIONS

The patient image (mammogram) is segmented into 2^m regions based on m level-set functions. After many attempts

(trial and error), the image intensity is divided to three nonparametric zones based on Oncologists and Radiologists experience. They say that the infected area always has high-intensity pixels in the mammogram images. Assume that the mammogram registered with 255 gray level, the first zone has 0-132 of grey level (GL), the second zone has 119-200 GL, and the third zone has184-255 GL. Each zone is divided to N unknown areas (more than 3 areas) and the nonparametric approach is applied on these zones to detect the breast cancer tumor. As one can see in Fig. 3, there are three intersection regions between zone 1 with zone 2, zone 2 with zone 3, and zone 1 with zone 3. These intersections are important to remove any noise or anything else between segmented zones. Also, to improve the borderlines detection among segmented regions which leads to enhanced breast cancer recognition in mammogram images based on curve evaluation.

To explain the main idea of the nonparametric approach let $m = 2$ in each zone, then, by equation (16), there are $2^m = 4$ conditional entropies to evaluate, namely

$$\hat{M}\left(F\left(Y\right)|L_{\vec{C}}\left(Y\right)=G_{++}\right),\ldots,\hat{M}\left(F\left(Y\right)|L_{\vec{C}}\left(Y\right)=G_{--}\right).$$

We calculate these estimations in a way analogous to what we have done in the case of two regions. For instance, $\hat{M}\left(F\left(Y\right)|L_{\vec{C}}\left(Y\right)=G_{++}\right)$ is determined by

$$\begin{aligned}\hat{M}&\left(F\left(Y\right)|L_{\vec{C}}\left(Y\right)=G_{++}\right)\\&=-\frac{1}{|G_{++}|}\int_{G_{++}}\log\hat{u}_{++}\left(F\left(y\right)\right)dy\\&\quad-\frac{1}{|G_{++}|}\int_{G_{++}}\log\left(\frac{1}{|G_{++}|}\int_{G_{++}}\left(V\left(F\left(y\right)\right.\right.\right.\\&\quad\left.\left.\left.-F\left(\hat{y}\right)\right)d\hat{y}\right)dy\end{aligned}\tag{17}$$

And the other entropy parameters are found in a similar manner. By utilizing the proposed multiphase technique, the first dissimilarity of the energy function $E(C)$ in the equation (13) is calculated as follows:

$$\begin{aligned}\frac{\partial\vec{C}_1}{\partial t}&=\vec{n}_1\left(\alpha k_1+H\left(Q_2\left(\vec{C}_1\right)\right)\left(\log\frac{\hat{u}_{++}\left(F\left(\vec{C}_1\right)\right)}{\hat{u}_{-+}\left(F\left(\vec{C}_1\right)\right)}\right.\right.\\&\quad+\frac{1}{|G_{++}|}\int_{G_{++}}\frac{K\left(F\left(y\right)-F\left(\vec{C}_1\right)\right)}{\hat{u}_{++}F\left(y\right)}dy\\&\quad\left.+\frac{1}{|G_{-+}|}\int_{G_{-+}}\frac{K\left(F\left(y\right)-F\left(\vec{C}_1\right)\right)}{\hat{u}_{-+}\left(F\left(y\right)\right)}dy\right)\\&\quad+\left(1-H\left(Q_2\left(\vec{C}_1\right)\right)\left(\log\frac{\hat{u}_{-+}\left(F\left(\vec{C}_1\right)\right)}{\hat{u}_{--}\left(F\left(\vec{C}_1\right)\right)}\right)\right.\\&\quad+\frac{1}{|G_{+-}|}\int_{G_{+-}}\frac{K\left(F\left(y\right)-F\left(\vec{C}_1\right)\right)}{\hat{u}_{\pm}\left(F\left(y\right)\right)}dy\\&\quad\left.-\frac{1}{|G_{--}|}\int_{G_{--}}\frac{K(F\left(y\right)-F(\vec{C}_1))}{\hat{u}_{--}(F\left(y\right))}dy\right)\end{aligned}\tag{18}$$

$$\begin{aligned}\frac{\partial\vec{C}_2}{\partial t}&=\vec{n}_2\left(\alpha k_2+H\left(Q_1\left(\vec{C}_2\right)\right)\left(\log\frac{\hat{u}_{++}\left(F\left(\vec{C}_2\right)\right)}{\hat{u}_{-+}\left(F\left(\vec{C}_2\right)\right)}\right.\right.\\&\quad+\frac{1}{|G_{++}|}\int_{G_{++}}\frac{K\left(F\left(y\right)-F\left(\vec{C}_2\right)\right)}{\hat{u}_{++}F\left(y\right)}dy\\&\quad\left.+\frac{1}{|G_{\mp}|}\int_{G_{\mp}}\frac{K\left(F\left(y\right)-F\left(\vec{C}_2\right)\right)}{\hat{u}_{\mp}\left(F\left(y\right)\right)}dy\right)\\&\quad+\left(1-H\left(Q_2\left(\vec{C}_2\right)\right)\left(\log\frac{\hat{u}_{-+}\left(F\left(\vec{C}_2\right)\right)}{\hat{u}_{--}\left(F\left(\vec{C}_2\right)\right)}\right)\right.\\&\quad+\frac{1}{|G_{+-}|}\int_{G_{+-}}\frac{K\left(F\left(y\right)-F\left(\vec{C}_2\right)\right)}{\hat{u}_{\pm}\left(F\left(y\right)\right)}dy\\&\quad\left.-\frac{1}{|G_{--}|}\int_{G_{--}}\frac{K\left(F\left(y\right)-F\left(\vec{C}_2\right)\right)}{\hat{u}_{--}\left(F\left(y\right)\right)}dp\right)\end{aligned}\tag{19}$$

The log-LA found in equations (18) and (19) checks the assumption that the density of the resulted mammogram $F(\vec{C}_i)$ at an identified pixel on the active borderline of the curve $\vec{C}_i$ belongs to one area or another. As shown in Fig. 4, $\vec{C}_i$ defines either the boundary between G_{++} and G_{-+}, or the boundary between G_{+-} and G_{--}, when $\vec{C}_1$ localizes inside or outside curvature $\vec{C}_2$, respectively. Equation (18) shows the regional competition between areas adjacent to curvature $\vec{C}_1$. Likewise, equation (19) shows the joined pixels among areas adjacent to curvature $\vec{C}_2$. For the intersection areas the pixels are ranked according to nonparametric memberships to decide which zone they belong to, so the tumor is easily found and the noise and distortion are removed from the image under consideration. This gives the ability to scan the medical image many times especially in the intersection areas.

B. PERFORMANCE EVALUATION OF MAMMOGRAM SEGMENTATION METHODS

To evaluate the performance of the proposed technique for the segmentation of mammogram images, the similarity is calculated by using Q, DSC, PSNR, HD, and PTD metrics. The segmented mammogram images resulting from the proposed technique and the segmented mammogram images produced by all other techniques cited in this paper are compared.

1) THE OVERALL IMAGE QUALITY

There are considerable parameters used to evaluate the segmentation performance comparison between the introduced method and the other segmentation approaches. It is recognized that individual areas in an image do not gather identical quantity of attention. In this paper we assumed that the total quality of the mammogram image Q is

$$Q=\frac{\sum_i w_i y_i}{\sum_i w_i}\tag{20}$$

Which is defined as the weighted local quality y_i of a region A_i with the corresponding local saliency w_i. There are many models of saliency discussed with different IQMs to improve prediction performance [30], [32]. Also, some parameters are famous like Dice Similarity Coefficient (DSC), peak signal-to-noise ratio (PSNR) metric, Haussdorff Distance (HD), and probability of tumor detection (PTD).

2) DICE SIMILARITY COEFFICIENT

The dice similarity coefficient (DSC) is used as a numerical substantiation metric to verify the reproducibility of breast cancer identification and the spatial overlap accuracy of the automated segmentation probabilistic of ROIs in mammogram images with both malignant and/or normal tissues. The Dice Similarity coefficient is a mathematical tool to determine which pixels represent a tumor tissue. Given two areas B_1, B_2 where B_1 is the area inside C_1 and B_2 is the area inside C_2, and the two areas differ in position but have the same circular shape [30], then $DSC \in [0, 1]$, is defined as:

$$\mathrm{DSC} = \frac{2\,(B_1 \cap B_2)}{B_1 + B_2} \tag{21}$$

The value of one for DSC means full consent and zero means no overlap at all.

3) PEAK SIGNAL-TO-NOISE RATIO (PSNR) METRIC

Peak signal-to-noise ratio (PSNR) metric is used to measure the quality of breast cancer recognition in mammogram images using different techniques [30]. PSNR defined as the ratio between the maximum possible value of a signal and the variable noise capacity (power of the changing noise) which affects the quality of its representation. Since many signals have an immersive dynamic range, the PSNR is usually represented in logarithmic decibels.

Therefore, to measure the ratio between the power of distorting noise and maximum value of pixel intensity PSNR is used. The PSNR is presented as terms of the logarithmic:

$$PSNR = 10 \log \left(\frac{(MI)^2}{\mathrm{D}(B_1, B_2)} \right) \tag{22}$$

where the maximum intensity value of the image is MI, $\mathrm{D}(B_1, B_2) = \frac{1}{m} \sum_{i=1}^{m} \left(X_i - \bar{X}_i\right)^2$, X_i is the vector of pixel density of the pixel actually expected. $\bar{X}_i$ is a vector of m points on all pixels produced unintentionally.

4) HUSSDORFF DISTANCE

The Haussdorff distance is used to measure the distance between the two subsections of the measuring space. The HD distance is the smallest distance between each point on the other side of the segment. This means that the side of one area of interest (ROIs) at each point refers to the smallest distance on the other side of the area of interest and the higher the distance HD of those values.

Therefore, the HD is used to define the smallest distance on the other side of desired area (infected region in mammogram) and the longest distance HD of these values.

$$HD = \max \left\{ \sup_{x \in A^*} \inf_{y \in A_*} D\,(x, y), \sup_{y \in A_*} \inf_{x \in A^*} D\,(x, y) \right\} \tag{23}$$

where $D\,(x, y) = |x - y|$.

5) MEAN-VARIANCE STANDARD DEVIATION AND EXPECTED VALUE OF BREAST CANCER DETECTION PROBABILITIES

Let $x_1, x_2, \cdots, x_s$ be a set of dissimilar random variables (a quantity having a numerical value for each patient of a group), the mean-value of the random variable x outlines where the density is positioned:

$$\mu = \frac{x_1 + x_2 + \cdots + x_N}{s} = \frac{1}{s} \sum_{i=1}^{s} x_i \tag{24}$$

Since the proposed method is applied to registered mammogram images (2D-greylevels), including nine sets of breast cancer images. Therefore, the pooled mean is as follows:

$$\mu = \sum_{i=1}^{s} x_i f_i\,(x) \tag{25}$$

where S defines the number of elements in the segmented mammogram. In addition, the variance is used to signify a measure of changeability of the variable in the resulted image as follow:

$$\sigma^2 = \sum_{i=1}^{S} (x - \mu_x)^2 f_i\,(x) \tag{26}$$

6) PROBABILITY OF TUMOR DETECTION

The probability of tumor detection (PTD) is used to measure the segmentation accuracy of the proposed technique (IBCNP) compared to the segmentation accuracy obtained from PDEs, IMBC, SDFs, and EINP. These techniques are applied to patient's images to get the probability of tumor detection in the original images (mammograms with high noise).

The metric PTD is used to calculate the possibility of tumor-detected cases among 159 cases used in this research.

$$PTD = \frac{Detected\ cases}{sum\ of\ all\ possiblecases} \times 100 \tag{27}$$

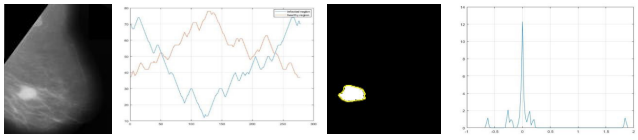

(a) Patient's Image (b) boundary of infected and healthy regions (c) resulted image (d) Log-AL for the ROI

FIGURE 5. The curve evolution on a mammogram image for set#1.

V. EXPERIMENTAL RESULTS

To test the proposed approach, a set of 156 real mammogram images were obtained from 9 different sets of patients with different sizes, dimensions, and types of breast cancer are used. In all sets, the regularization parameters in equations (9) or (13), were exclusively chosen and categorized based on the

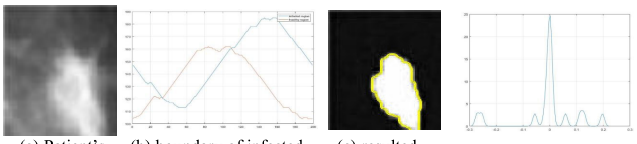

FIGURE 6. The curve evolution on a mammogram image for set#2.

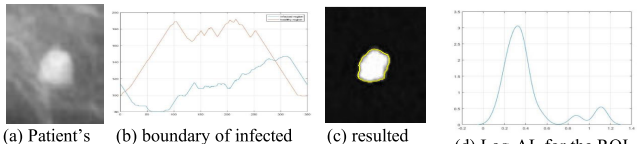

FIGURE 7. The curve evolution on a mammogram image for set#3.

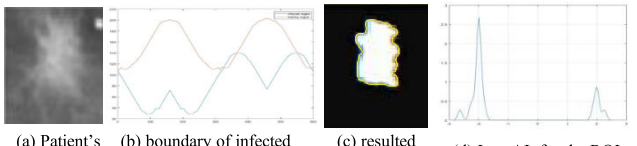

FIGURE 8. The curve evolution on a mammogram image for set#4.

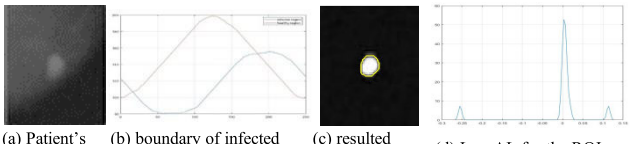

FIGURE 9. The curve evolution on a mammogram image for set#5.

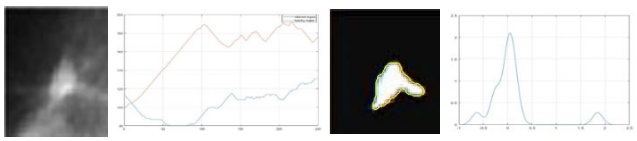

FIGURE 10. The curve evolution on a mammogram image for set#6.

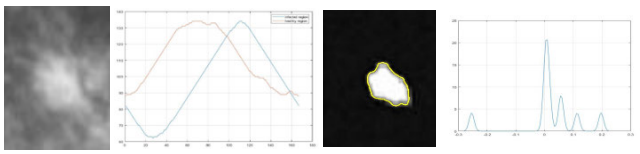

FIGURE 11. The curve evolution on a mammogram image for set#7.

value of qualitative estimation in segmenting mammogram. In sets where information is available about breast cancer in the mammogram, it is probable to get a suitable distribution function of datasets as an integral equal to a desired value based on the recognized features of cancer tissue borders combined with the signal to noise ratio (SNR) of the segmented mammograms. To illustrate the proposed technique, Figs. 5-13 demonstrate the results of the segmentation for sets 1-9 where the foreground (desired object) and background have Gaussian distributions with different mean-values and

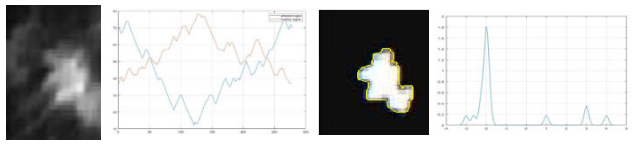

FIGURE 12. The curve evolution on a mammogram image for set#8.

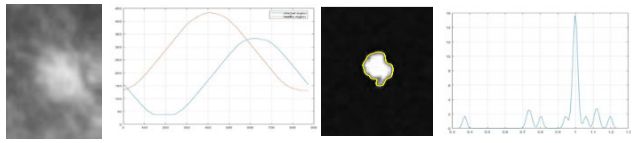

FIGURE 13. The curve evolution on a mammogram image for set#9.

equal variance. Generally, up to 64 % of mass can be identified during mammography examination. These types of modalities include a topological retraction where the white-area is within the grey-area and not only the complicated borders. The proposed multi-phase identification technique can overcome current problems such as the topological problems, recognition of the white-area, the background, and the grey-area. Fig. 5(a)-13(a) show initial images with both infected and healthy regions. For this type of mammogram with a simple initialization, it leads to several iterations and a few sets of unterminated curvature at a limited optimal. The multiple configuration power is that all regions are achieved, and the curvature estimation happens entirely. Fig. 5(b)-13(b) present boundaries between infected region (G_i) and healthy region (G_j) in mammogram. The boundary of infected and healthy regions is detected after the proposed method has been applied to the mammogram images of the first set. The boundary of infected and healthy regions is detected using the nonparametric algorithm based on image pixel intensities to identify any of the pixels from healthy tissues and that containing malignant tissues. The main advantage of the proposed method is that it describes infected area in efficient borderlines and is relatively unaffected by mammogram noise. Therefore, the pixels at which mammogram intensities change sharply are typically grouped into sets of curved borderline segments. Fig. 5(c)-13(c) show segmented ROI (region of interested or infected region) with boundary after applying the proposed algorithm. A pixel in the infected region (G_i) of (G_{mn}, u_{mn}) is linked to the pixel at (G_{mn}, u_{mn}) if both pixel intensity and direction criteria of the energy function $E(C)$ are satisfied. This means that $\vec{C}_1$ localizes inside curvature $\vec{C}_2$. So, automatic initialization of one mass (segmented-ROI) has been detected with boundary in mammograms as shown in Fig. 5(c)-13(c). Fig. 5(d)-13(d) provide the Log-AL results of the ROI for all ninth sets, which decides whether the detected mass is normal or malignant. For each pixel in the Cartesian mammogram plane the value of the Log-AL is calculated for various values of the gradient-flow ($ak\vec{n}$) for the length of the curvature and the curve

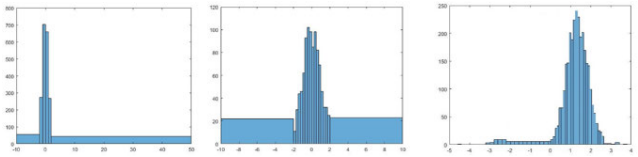

(a) The first term for all the pixels along the borderlines of mammogram

(b) Second and third terms for all the pixels along the borderlines of mammogram

(c) Log-AL for all the pixels along the borderlines of mammogram

FIGURE 14. Histogram results of the gradient flow terms for the objects in mammogram images of Figures 5 to 13.

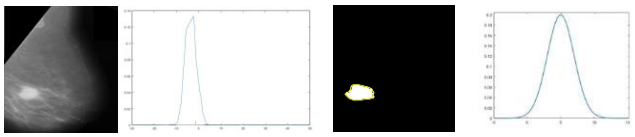

(a) Patient's Image (b) i_1 (c) With boundary (d) i_2

FIGURE 15. Results of the proposed method for the first set of samples: (a) Initial image with both malignant and/or normal; (b) the object with density i_1; (c) segmented image with boundary; (d) the background with density i_2.

dimensions (k) using the log-based in equations (18) and (19). The histograms achieved by the Log-AL indicate that all the values obtained during the curve evaluation process with the datasets have limited range between −2.7 and 3.8. This technique assumes that there are collinear pixels lying on a line between foreground and background, this leads to the resulting curve has borderline which intersects at (G_{mn}, u_{mn}) in the parametric domain, which precisely recognizes the malignant mass in the mammogram.

VI. CASE STUDY

The proposed technique is applied to many different patient images with both malignant and/or normal tissues to show its capability in the identification process. The existing results were acquired using an improved nonparametric approach based on image pixel intensities for 156 real data sets. To exemplify the introduced method, the presented technique is applied to many of the mammogram images with normal and abnormal tissues as already described in this research. This algorithm uses the log-based in equations (18) and (19) in the analysis process. To show the importance of using the three expressions in equation (16), all the data obtained is summarized during the curve estimation process with the datasets. Fig.14 shows histogram results of the gradient flow terms for the objects in mammogram images of Figs. 5 to13. Their histograms in Fig.14 show its importance in calculations. Fig. 14 (a) presents histograms achieved by the first term of the log-based in equation (16) of data. It is found that values of first terms are often close to 1 and are of limited value (especially between −2 and 3.5). Fig. 14(b) shows histograms resulted from the difference between the second term and the third term of log-based in equation (16). Consequently, both terms have a limited range, their variances also have a limited value (especially between –2.7 and +3.8). Lastly, Fig. 14(c) shows a histogram resulted from log-AL. It can be seen that predominantly equations (18) and (19) are larger magnitude than the second term and third term in equation (17) and their variance. Consequently, it is the prominent provider of curve evaluation. Figs. 15-23 show the results of the introduced technique for mammogram images from the 9 sets. To help the reader understand the capability of the proposed technique in breast cancer recognition and segmentation processes, the main outlines of the experimental results using the improved-nonparametric approach based on image pixel intensities and curve estimation in Figs. 15-23 are illustrated.

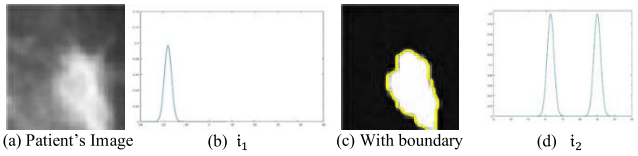

(a) Patient's Image (b) i_1 (c) With boundary (d) i_2

FIGURE 16. Results of the proposed method for the second set of samples: (a) Initial image with both malignant and/or normal; (b) the object with density i_1; (c) segmented image with boundary; (d) the background with density i_2.

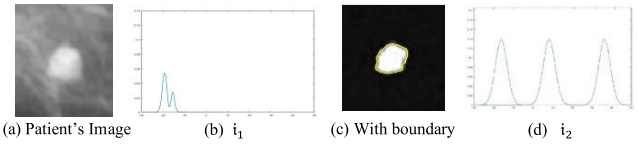

(a) Patient's Image (b) i_1 (c) With boundary (d) i_2

FIGURE 17. Results of the proposed method for the third set of samples: (a) Initial image with both malignant and/or normal; (b) the object with density i_1; (c) segmented image with boundary; (d) the background with density i_2.

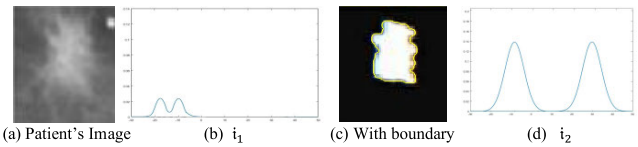

(a) Patient's Image (b) i_1 (c) With boundary (d) i_2

FIGURE 18. Results of the proposed method for the fourth set of samples: (a) Initial image with both malignant and/or normal; (b) the object with density i_1; (c) segmented image with boundary; (d) the background with density i_2.

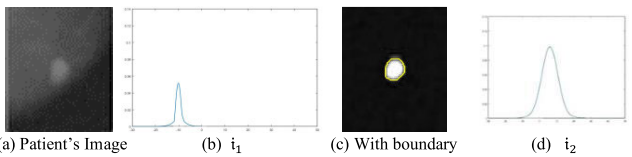

(a) Patient's Image (b) i_1 (c) With boundary (d) i_2

FIGURE 19. Results of the proposed method for the fifth set of samples: (a) Initial image with both malignant and/or normal; (b) the object with density i_1; (c) segmented image with boundary; (d) the background with density i_2.

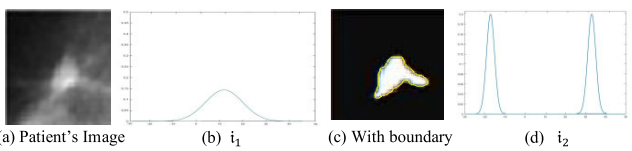

(a) Patient's Image (b) i_1 (c) With boundary (d) i_2

FIGURE 20. Results of the proposed method for the sixth set of samples: (a) Initial image with both malignant and/or normal; (b) the object with density i_1; (c) segmented image with boundary; (d) the background with density i_2.

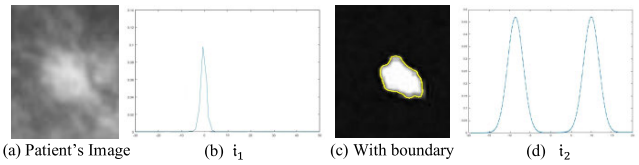

FIGURE 21. Results of the proposed method for the seventh set of samples: (a) Initial image with both malignant and/or normal; (b) The object with density i_1; (c) Segmented image with boundary; (d) The background with density i_2.

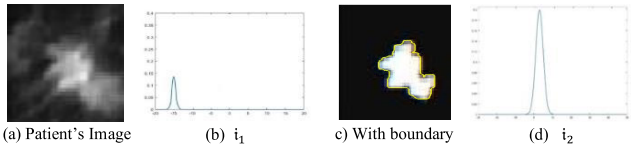

FIGURE 22. Results of the proposed method for the eighth set of samples: (a) Initial image with both malignant and/or normal; (b) the object with density i_1; (c) segmented image with boundary; (d) the background with density i_2.

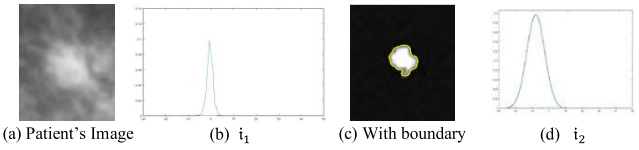

FIGURE 23. Results of the proposed method for the ninth set of samples: (a) Initial image with both malignant and/or normal; (b) the object with density i_1; (c) segmented image with boundary; (d) the background with density i_2.

Figures 15 (a)-23(a) show the patient's image with both malignant and/or normal regions as obtained from the first set of the nine sets. The fundamental object and integrated background disseminations are a bilateral intensity with Gaussian intensity distribution and two Gaussian components as shown in Figs. 15(b)-23(b) and Figs. 15(d)-23(d), respectively. Both disseminations have the same mean-variance and mean-value (the same diameter), making it difficult for a radiologist's visual system to distinguish the object from the background. To show the foreground view, the real boundary lines are shown by the curve in Figs. 15(c)-23(c).

VII. DISCUSSIONS RESULTS

The proposed method is applied to more difficult mammograms with both malignant and/or normal tissues present to confirm its proficiency in the segmentation process. Figs. 24(a)-31(a) show the patient images contain foreground and background including noise as a white colour within the grayscale area, which makes it difficult to detect abnormalities in this image. That's why the radiologists say that it's a difficult image because this type of mammogram contains not only invisible/unclear borders, but additionally a quantum noise that white area is within the grayscale area, resulting in a significant impact on image analysis and accuracy of segmentation. The pixel distributions of the initial objective and combined background are a two-sided intensity with a numerical distribution of Gaussian density and two modules

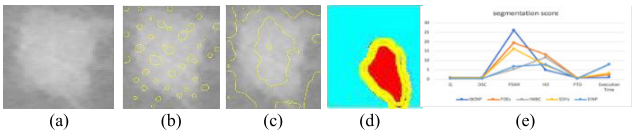

FIGURE 24. The curve evolution on a mammogram image for set#1: (a) Patient's image, (b) First stage, (c) Intermediate stage, (d) Final stage, (e) Quality of segmentation.

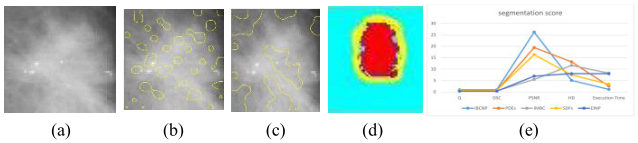

FIGURE 25. The curve evolution on a mammogram image for set#2: (a) Patient's image, (b) First stage, (c) Intermediate stage, (d) Final stage, (e) Quality of segmentation.

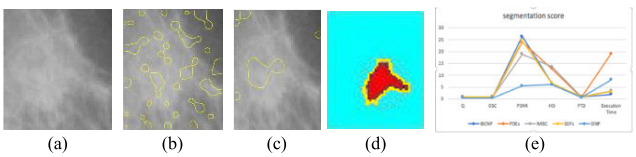

FIGURE 26. The curve evolution on a mammogram image for set#3: (a) Patient's image, (b) First stage, (c)Intermediate stage, (d) Final stage, (e) Quality of segmentation.

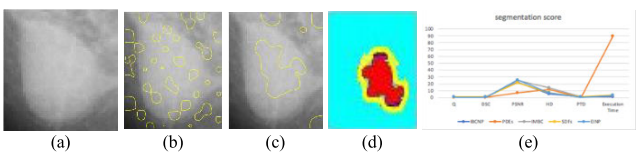

FIGURE 27. The curve evolution on a mammogram image for set#4: (a) Patient's image, (b) First stage, (c) Intermediate stage, (d) Final stage, (e) Quality of segmentation.

of Gaussian. Therefore, it is challenging for the radiologist's visual system to distinguish/identify the ROI from the background because the distributions have the same mean-values and variance. The presented method can handle and resolve this problem and the four regions capture the background, the foreground, the area with white colour, and the area with greyscale level. To give the reader an objective view about the complexity of the proposed algorithm, real examples of breast cancer detection using the proposed algorithm are demonstrated next. The patient's images that were obtained from the nine sets of samples contain a very small area of breast cancer as shown in Figs. 24 (a)-31(a). In these sets, there are two forms of Gaussian (unimodal and bi-modal) intensities with two Gaussian constituents for the fundamental foreground and background disseminations, as shown Figs. 24 (b)-31(b), and Figs. 24(c)-31(c). It was found that both Gaussian distributions have a similar mean-value and mean-variance, thus it is difficult for radiologists and/or oncologist visual systems to distinguish the object from the background. Figures 24(c)-31(c) show the results of the ROI for all ninth sets, which present segmented images with boundary. For this sample of mammogram images with simple initialization image types as shown in Figs. 24- 31, much iterations and

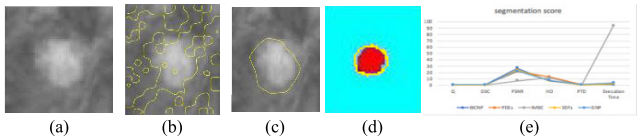

FIGURE 28. The curve evolution on a mammogram image for set#5: (a) Patient's image, (b) First stage, (c) Intermediate stage, (d) Final stage, (e) Quality of segmentation.

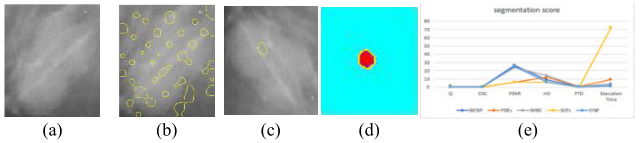

FIGURE 29. The curve evolution on a mammogram image for set#6: (a) Patient's image, (b) First stage, (c) Intermediate stage, (d) Final stage, (e) Quality of segmentation.

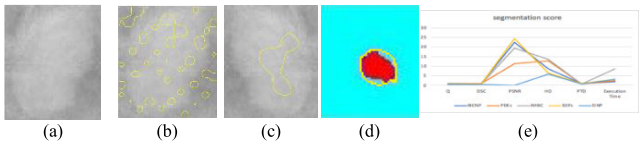

FIGURE 30. The curve evolution on a mammogram image for set#7: (a) Patient's image, (b) First stage, (c) Intermediate stage, (d) Final stage, (e) Quality of segmentation.

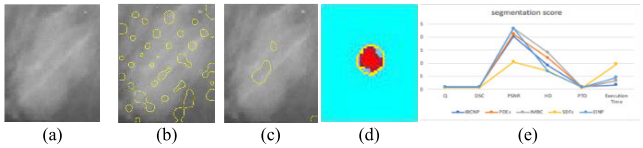

FIGURE 31. The curve evolution on a mammogram image for set#8: (a) Patient's image, (b) First stage, (c) Intermediate stage, (d) Final stage, (e) Quality of segmentation.

in some cases the curve may be captured in a local optimal zone. The power of multi-initialization is that all regions are achieved and the curve estimation is completed. The figures illustrate the intermediate stages of assessment at which seeds in the background area are regularly analysed at each stage, while seeds in the area of the object grow. Figs. 24(d) to 31(d) provide a segmentation result for all sets. In these figures, the last curvature includes the core of the malignant tissues (resulted area). Figs. 24 (e) to 31 (e) demonstrate the efficiency of the proposed method (IBCNP) for measuring the quality of segmentation process. The mammograms of the nine sets of patients with different sizes, dimensions, and types of breast cancer are used to assess the effectiveness of the proposed technique by assessing the segmentation quality as compared to the other four different segmentation techniques (PDEs, IMBC, SDFs, and EINP). Five segmentations of given mammogram images generated by five methods with different parameters are shown in Figs. 24 (e) to 31(e). The plots of the segmentation results that were obtained from 156 subjects show that the IBCNP method has the best segmentation quality.

VIII. PERFORMANCE DISCUSSIONS AND COMPARATIVE RESULTS

A comparative study is performed using different mammogram image segmentation techniques to evaluate the performance of the proposed one. The results obtained from the proposed algorithm are compared to those produced by four different popular segmentation techniques (PDEs, IMBC, SDFs, and EINP). The initially processed segmented images are divided into three nonparametric zones based on pixel intensity, and then each zone is segmented to N unclassified areas. The proposed technique is applied to these zones to detect the malignant tissues in mammograms. The accuracy of the identification process is obtained by comparing the resulting images from different segmentation techniques as applied to mammogram images with different sizes, dimensions, and types of breast malignant tissues using the overall mammogram image quality (Q), the Dice similarity coefficient (DSC), Peak signal-to-noise ratio (PSNR) metric, Haussdorff Distance (HD) and probability of tumor detection (PTD). Also, the comparison involves measuring the average execution time of each technique in seconds as listed in Tables 1-3 for all of the nine sets. The DSC is used as a statistical validation metric to estimate the performance of both the reproducibility of borderlines of the desired area in segmented images and the spatial overlap accuracy of automated probabilistic subdividing of mammogram images (foreground and background). The DSC is obtained by using equation (21). The Q is obtained by using equation (20), PSNR metric is obtained by using equation (22), HD is obtained by using equation(23), and the probability of tumor detection (PTD) is obtained by using equation (27). The Q, PSNR, HD, and PTD values were calculated, and the mean values of logarithmic transformed values were compared with the analysis of variance. Table 1 shows the comparative results of the breast cancer segmentation process on nine sets of mammogram images using the proposed technique (IBCNP) and four other different segmentation techniques (PDEs, IMBC, SDFs, and EINP). In this table, the comparison of the speed of the breast cancer identification process has been calculated using the average execution time in seconds. The breast cancer segmentation methods similarity measurements show that Q, DSC, PSNR, HD and PTD measurements of IBCNP are better than the equivalent measurements in the case of the PDEs, IMBC, SDFs, and EINP methods. This indicates that the IBCNP method is the most precise segmentation method among all the methods mentioned above. Table 2 shows the result of the mean-variance standard deviation and expected value of breast cancer detection probabilities of the proposed technique in the nine sets. As can be seen in Table 2 for all cases, the average and standard deviation of the proposed algorithm are $\mu = 0.397815$ and, $\sigma = 0.260253$, where the mean and standard deviation are obtained by using equations (25) and (26). The mean and standard deviation for the ROIs are $\mu = 0.029141$ and, $\sigma = 0.017924$. As shown in Table 2,

TABLE 1. Comparative results of breast cancer identification on 9 sets with both malignant and/or normal using different techniques.

No. of Set	Identification Techniques	Q	DSC	PSNR	HD	PTD	Average Execution Time
Set #1	**IBCNP**	**0.942**	**0.981**	**26.20**	**5.04**	**0.892**	**1.1237**
	PDEs	0.631	0.622	19.44	13.17	0.731	2.5670
	IMBC	0.507	0.495	5.47	11.61	0.607	8.2237
	SDFs	0.731	0.727	16.34	7.491	0.751	3.3737
	EINP	0.334	0.325	6.90	8.006	0.434	7.9726
Set #2	**IBCNP**	**0.933**	**0.956**	**23.94**	**6.64**	**0.952**	**1.1603**
	PDEs	0.915	0.976	19.56	11.97	0.815	3.2837
	IMBC	0.881	0.983	23.64	13.91	0.781	3.1037
	SDFs	0.461	0.454	5.349	6.431	0.561	8.1470
	EINP	0.504	0.495	19.04	6.116	0.604	3.5503
Set #3	**IBCNP**	**0.952**	**0.914**	**26.34**	**6.44**	**0.943**	**1.8493**
	PDEs	0.723	0.713	23.93	12.77	0.693	18.963
	IMBC	0.852	0.943	18.86	13.61	0.837	3.3303
	SDFs	0.825	0.813	24.55	6.531	0.785	3.0403
	EINP	0.434	0.424	5.446	5.916	0.534	8.0903
Set #4	**IBCNP**	**0.961**	**0.886**	**22.61**	**5.09**	**0.953**	**1.0803**
	PDEs	0.317	0.304	6.844	11.89	0.517	89.367
	IMBC	0.728	0.713	25.10	14.01	0.828	2.1337
	SDFs	0.891	0.934	21.66	6.982	0.791	3.2737
	EINP	0.767	0.747	25.78	6.881	0.669	3.0370
Set #5	**IBCNP**	**0.946**	**0.928**	**26.76**	**7.013**	**0.986**	**1.0003**
	PDEs	0.768	0.986	21.52	13.17	0.898	3.4903
	IMBC	0.339	0.324	6.966	11.61	0.539	93.780
	SDFs	0.768	0.747	24.14	7.489	0.662	2.1237
	EINP	0.815	0.976	22.38	8.081	0.795	3.9703
Set #6	**IBCNP**	**0.961**	**0.948**	**26.51**	**8.694**	**0.951**	**1.3170**
	PDEs	0.649	0.629	6.095	11.97	0.674	9.3870
	IMBC	0.878	0.863	23.78	13.91	0.698	3.9737
	SDFs	0.409	0.389	6.199	6.403	0.607	72.423
	EINP	0.168	0.054	25.01	6.102	0.568	2.0870
Set #7	**IBCNP**	**0.946**	**0.934**	**22.39**	**8.494**	**0.972**	**1.9537**
	PDEs	0.747	0.986	11.29	12.77	0.847	2.5603
	IMBC	0.649	0.634	19.52	13.61	0.749	8.6937
	SDFs	0.839	0.817	24.25	6.503	0.879	3.1903
	EINP	0.375	0.364	15..8	5.902	0.675	3.0847
Set #8	**IBCNP**	**0.953**	**0.943**	**20.21**	**9.109**	**0.925**	**1.6437**
	PDEs	0.814	0.802	21.15	11.89	0.794	3.3070
	IMBC	0.745	0.731	23.37	14.01	0.655	3.2503
	SDFs	0.597	0.584	10.51	6.908	0.601	9.7270
	EINP	0.863	0.855	23.29	6.808	0.762	4.5537
Set #9	**IBCNP**	**0.954**	**0.976**	**26.96**	**22.05**	**0.949**	**1.6630**
	PDEs	0.268	0.248	13.54	27.18	0.768	92.953
	IMBC	0.642	0.634	21.69	10.62	0.542	3.3603
	SDFs	0.783	0.769	22.07	6.50	0.683	3.5270
	EINP	0.594	0.578	10.33	7.01	0.648	10.457

TABLE 2. The result of the mean and standard deviation of the nonparametric approach on 9 sets with both malignant and/or normal.

No. of Sets		Patient's Images	Segmented Images
Set#1	μ	0.426225	0.037952
	σ	0.348904	0.032801
Set#2	μ	0.204086	0.023034
	σ	0.218341	0.024035
Set#3	μ	0.425384	0.037993
	σ	0.348907	0.037987
Set#4	μ	0.204694	0.023053
	σ	0.218601	0.023951
Set#5	μ	0.426849	0.038801
	σ	0.348906	0.038101
Set#6	μ	0.204867	0.023069
	σ	0.218331	0.023963
Set#7	μ	0.427557	0.037986
	σ	0.349745	0.038157
Set#8	μ	0.205289	0.023045
	σ	0.218273	0.023695
Set#9	μ	0.428097	0.037796
	σ	0.351888	0.038096

TABLE 3. Average comparative results of breast cancer detection on 9 sets with both malignant and/or normal using different approaches.

All Sets	Identification Techniques	Q	DSC	PSNR	HD	PTD	Average Execution Time
Average results	**IBCNP**	**0.94937**	**0.934**	**22.39**	**8.494**	**0.96841**	**1.9537**
	PDEs	0.74798	0.986	11.29	12.77	0.80721	2.5603
	IMBC	0.64969	0.634	19.52	13.61	0.75693	8.6937
	SDFs	0.83975	0.817	24.25	6.503	0.82867	3.1903
	EINP	0.37594	0.364	15..8	5.902	0.72583	3.0847

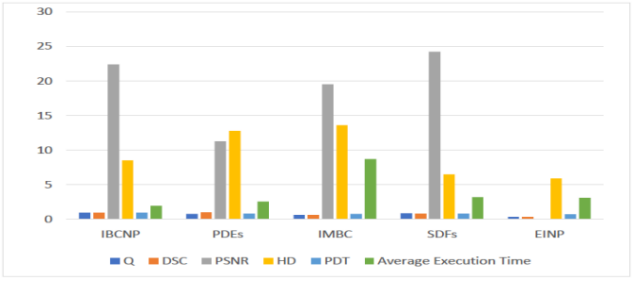

FIGURE 32. Q, DSC, PSNR, HD, and PTD comparison results on 9 sets with both malignant and/or normal using IBCNP, PDEs, IMBC, SDFs, and EINP.

the mean-variance standard deviation of the proposed technique is very sensitive to the region of malignant tissues and the recognition of breast cancer is very sensitive. As shown in Tables 3, identification of breast cancer in mammogram images using the proposed technique is more robust compared to the others four techniques. Fig. 32 shows the comparison of similarity throughout the breast cancer segmentation results using the five different techniques of image segmentation as applied to the nine sets. These outcomes are schemed in column charts to illustrate the comparative results of breast cancer segmentation among the IBCNP, PDEs, IMBC, SDFs, and EINP segmentation techniques using Q, DSC, PSNR, HD, and PTD similarities. Computation speed comparison is achieved using the mean value of performance time in seconds. These results indicate that the proposed method (IBCNP) has the smallest bar graph that denotes

the highest speed with high accuracy in the segmentation approach. Finally, based on results, it can be determined that the proposed method has high values of Q, DSC, PSNR, PTD, and the lowest HD that denotes high accuracy and fastest speed in the segmentation process.

IX. CONCLUSION

In analyzing medical images, radiologists face a problem with the differentiation between benign and malignant tissues in mammogram images due to the white area being within the grey area that leads to difficulty of a direct diagnosis of the breast cancer. Up to 64 % of breast cancers usually can be detected in mammogram images as a mass, but practically, it is difficult to identify most tumor size smaller than 4.9 mm^3. The threshold for recognition of a tumor depends on the tissue density, examination quality, radiographic irregularity, and the experience of the radiologist. The proposed multi-phase segmentation technique can help solve this issue, and the three portions handle the grey region, white region and background. In this paper, we presented a nonparametric approach based on the curve estimation technique to the problem of mammographic image segmentation with a data-theoretic perspective. The proposed method formulates the segmentation problem by maximizing mutual data between area identifiers and pixel intensities. We obtained the curve estimation equations for the image improvement problem modeled in the frame of the image. Due to the non-parametric feature of our methodology, the presented approach is capable of robotically managing several image segmentation problems where many currently available curve estimation methods fail completely or require at least statistical extraction for each zone. In this research, a comparative study has been conducted between different mammogram image segmentation methods to determine the most accurate segmentation methods. The performance of the proposed segmentation method is estimated and compared with PDEs, IMBC, SDFs, and EINP segmentation methods using several important image quality counters such as Q, DSC, PSNR, HD, and PTD. Also, the execution time for each segmentation technique is measured to determine the speed of the segmentation process as an additional performance indicator. In this work, a precise approach was used to compute the curve and non-parametric estimation that keep the computational difficulties at a reasonable level. A segmentation approach to differentiate between carcinoma and non-tumorous tissues for breast cancer is presented. This approach prepares the theoretical problem of data optimization by applying curve estimation techniques and deriving the correlated gradient flows. To attain the evolution that results, level-set techniques were used. In addition, it is based on the evaluation of mutual data and non-parametric density, considering the calculation of histograms, variances, averages and determinants of covariance matrices. The introduced technique was applied to mammograms having more than two regions of interest and including the use of spatially dependent probability density functions. The results showed the quality of the approach presented in the precise segmentation of real mammogram images. The proposed algorithm improved accuracy with agreement with the radiologist expert's assessments.

REFERENCES

[1] C. E. DeSantis, J. Ma, A. G. Sauer, L. A. Newman, and A. Jemal, "Breast cancer statistics, 2017, racial disparity in mortality by state," *CA, A Cancer J. Clinicians*, vol. 67, no. 6, pp. 439–448, 2017.
[2] K. Abernathy, Z. Abernathy, A. Baxter, and M. Stevens, "Global dynamics of a breast cancer competition model," *Differ. Equ. Dyn. Syst.*, vol. 17, no. 346, pp. 1–15, Jan. 2017.
[3] G. Y. Cho, L. Moy, J. L. Zhang, S. Baete, R. Lattanzi, M. Moccaldi, J. S. Babb, S. Kim, D. K. Sodickson, and E. E. Sigmund, "Comparison of fitting methods and b-value sampling strategies for intravoxel incoherent motion in breast cancer," *Magn. Reson. Med.*, vol. 74, no. 4, pp. 1077–1085, 2015.
[4] H. Knútsdóttir, E. Pálsson, and L. Edelstein-Keshet, "Mathematical model of macrophage-facilitated breast cancer cells invasion," *J. Theor. Biol.*, vol. 357, pp. 184–199, Sep. 2014.
[5] A. Simmons, P. M. Burrage, D. V. Nicolau. Jr., S. R. Lakhani, and K. Burrage, "Environmental factors in breast cancer invasion: A mathematical modelling review," *Pathology*, vol. 49, no. 2, pp. 172–180, 2017.
[6] M. Colom, M. Lebrun, A. Buades, and J. M. Morel, "A non-parametric approach for the estimation of intensity-frequency dependent noise," in *Proc. IEEE Int. Conf. Image Process. (ICIP)*, Oct. 2014, pp. 4261–4265.
[7] S. Diamantas and K. Alexis, "Modeling pixel intensities with log-normal distributions for background subtraction," in *Proc. IEEE Int. Conf. Imag. Syst. Techn. (IST)*, Oct. 2017, pp. 1–6.
[8] W. R. Schwartz, D. Balbino, E. R. Nascimento, and W. R. Schwartz, "A non-parametric approach to detect changes in aerial images," in *Progress in Pattern Recognition, Image Analysis, Computer Vision, and Applications (CIARP)*, vol. 9423. Montevideo, Uruguay: Springer, Nov. 2015, p. 116.
[9] O. Ronneberger, P. Fischer, and T. Brox, "U-Net: Convolutional networks for biomedical image segmentation," in *Proc. Int. Conf. Med. Image Comput. Comput.-Assist. Intervent.* Cham, Switzerland: Springer, 2015, pp. 234–241.
[10] A. Farag, L. Lu, H. R. Roth, J. Liu, E. Turkbey, and R. M. Summers, "A bottom-up approach for pancreas segmentation using cascaded superpixels and (deep) image patch labeling," *IEEE Trans. Image Process.*, vol. 26, no. 1, pp. 386–399, Jan. 2017.
[11] M. A.-M. Salem, A. Atef, A. Salah, and M. Shams, "Recent survey on medical image segmentation," in *Handbook of Research on Machine Learning Innovations and Trends*. Hershey, PA, USA: IGI Global, 2017, pp. 424–464.
[12] M. Chini, R. Hostache, L. Giustarini, and P. Matgen, "A hierarchical split-based approach for parametric thresholding of SAR images: Flood inundation as a test case," *IEEE Trans. Geosci. Remote Sens.*, vol. 55, no. 12, pp. 6975–6988, Dec. 2017.
[13] Z. Zhou, Y. Wang, Q. M. J. Wu, C.-N. Yang, and X. Sun, "Effective and efficient global context verification for image copy detection," *IEEE Trans. Inf. Forensics Security*, vol. 12, no. 1, pp. 48–63, Jan. 2017.
[14] S. Niu, Q. Chen, L. de Sisternes, Z. Ji, Z. Zhou, and D. L. Rubin, "Robust noise region-based active contour model via local similarity factor for image segmentation," *Pattern Recognit.*, vol. 61, pp. 104–119, Jan. 2017.
[15] G. Jordan, A. Petrik, B. De Vivo, S. Albanese, A. Demetriades, and M. Sadeghi, "GEMAS: Spatial analysis of the Ni distribution on a continental-scale using digital image processing techniques on European agricultural soil data," *J. Geochem. Explor.*, vol. 186, pp. 143–157, Mar. 2018.
[16] A. Taruttis and V. Ntziachristos, "Advances in real-time multispectral optoacoustic imaging and its applications," *Nature Photon.*, vol. 9, no. 4, p. 219, 2015.
[17] C. Li, C.-Y. Kao, J. C. Gore, and Z. Ding, "Minimization of region-scalable fitting energy for image segmentation," *IEEE Trans. Image Process.*, vol. 17, no. 10, pp. 1940–1949, Oct. 2008.
[18] S. J. S. Gardezi, A. Elazab, B. Lei, and T. X. Wang, "Breast cancer detection and diagnosis using mammographic data: Systematic review," *J. Med. Internet Res.*, vol. 21, no. 7, 2019, Art. no. e14464.

[19] H. Li, K. R. Mendel, L. Lan, D. Sheth, and M. L. Giger, "Digital mammography in breast cancer: Additive value of radiomics of breast parenchyma," *Radiology*, vol. 291, no. 1, pp. 15–20, 2019.

[20] G. B. Junior, S. V. da Rocha, J. D. S. de Almeida, A. C. de Paiva, A. C. Silva, and M. Gattass, "Breast cancer detection in mammography using spatial diversity, geostatistics, and concave geometry," *Multimedia Tools Appl.*, vol. 78, no. 10, pp. 13005–13031, 2019.

[21] J. Kim, J. W. Fisher, A. Yezzi, M. Cetin, and A. S. Willsky, "A nonparametric statistical method for image segmentation using information theory and curve evolution," *IEEE Trans. Image Process.*, vol. 14, no. 10, pp. 1486–1502, Oct. 2005.

[22] Y. Wang and C. He, "Adaptive level set evolution starting with a constant function," *Appl. Math. Model.*, vol. 36, no. 7, pp. 3217–3228, 2012.

[23] J. Lie, M. Lysaker, and X.-C. Tai, "A piecewise constant level set framework," *Int. J. Numer. Anal. Model.*, vol. 2, no. 4, pp. 422–438, 2005.

[24] E. E. M. Azhari, M. M. M. Hatta, Z. Z. Htike, and S. L. Win, "Brain tumor detection and localization in magnetic resonance imaging," *Int. J. Inf. Technol. Converg. Services*, vol. 4, no. 1, pp. 1–11, 2014.

[25] X.-C. Tai and H. Li, "A piecewise constant level set method for elliptic inverse problems," *Appl. Numer. Math.*, vol. 57, nos. 5–7, pp. 686–696, 2007.

[26] X. Zhang, J. Sun, S. Lu, and G. Wang, "Non-parametric detector in non-homogeneous clutter environments with knowledge-aided permutation test," *IET Radar, Sonar Navigat.*, vol. 10, no. 7, pp. 1310–1318, 2016.

[27] J. L. Sanz-Gonzalez, F. Alvarez-Vaquero, and J. E. Gonzalez-Garcia, "Permutation test algorithms for nonparametric radar detection," in *Proc. IET Int. Conf. Radar Syst.*, Oct. 2007, pp. 1–5.

[28] T. Kypraios and P. D. O'Neill, "Bayesian nonparametrics for stochastic epidemic models," *Stat. Sci.*, vol. 33, no. 1, pp. 44–56, 2018.

[29] P. R. White, "Non-parametric techniques for the estimation of spatial spectra in non-stationary environments," *IET Radar, Sonar Navigat.*, vol. 1, no. 3, pp. 184–190, Jun. 2007.

[30] G. G. N. Geweid, M. A. Elsisy, O. S. Faragallah, and R. Fazel-Razai, "Efficient tumor detection in medical images using pixel intensity estimation based on nonparametric approach," *Expert Syst. Appl.*, vol. 120, no. 1, pp. 139–154, 2019.

[31] E. Kowsari, B. Safarinejadian, and J. Zarei, "Non-parametric fault detection methods in non-linear systems," *IET Sci., Meas. Technol.*, vol. 10, no. 3, pp. 167–176, 2016.

[32] X. Shang, X. Zhao, and Y. Ding, "Image quality assessment based on joint quality-aware representation construction in multiple domains," *J. Eng.*, vol. 2018, Mar. 2018, Art. no. 1214697.

GAMAL G. N. GEWEID is currently a Postdoctoral Research Fellow with the Electrical Engineering Department, School of Electrical Engineering and Computer Science, University of North Dakota, ND, USA. Dr. Geweid has a solid background in physics, mathematics, biology, radiology and imaging sciences, and strong programming skills in MATLAB, Python, and C++ programming languages. He has a record of research publications and has excellent oral and written English communication skills. He is also a very strong and professionally sound academic background in digital image processing, signal processing, multimodality medical imaging (ultrasound, PET/CT, and MRI), CT image reconstruction, nanorobots in medicine, high-resolution MR imaging, mechatronics, medicalrobotics, biomedical instrumentation, computer vision, pattern recognition, software reliability and modeling, biosensors, and imaging and information technology in biomedicine. He has extensive working experience with electronic health records (EHRs). He used patient information to improve the ability to diagnose diseases and reduce-even prevent-medical errors leading to improved patient outcomes. He is developing novel high-resolution and fast imaging methods for neurological diseases, developing diagnostic tools, establishing risk stratification algorithms, and developing new tools for detecting chronic diseases in early stages. He has a record of research publications and four patents (surgical and diagnostic devices), all in the field of biomedicine, and he applied all of them to the real patients. He also has experience and interest in using deep learning, machine learning, bioinformatics, signal processing in epidemiology, and other relevant topics.

MAHMOUD A. ABDALLAH received the Ph.D. degree in systems engineering from The University of Toledo,Toledo, OH, USA, in 1986, and is licensed Professional Engineer (PE) by the State of Ohio. He is currently a Professor of manufacturing engineering with Central State University. His research interests include image and signal processing, space-time adaptive processing (STAP), multiscale image compression, pattern recognition, machine learning, artificial intelligence and expert system applications in diagnostic systems, multijoint manipulators design and control, and imbedded systems.